Superimposed Sacrificial Texturing to Enhance the Optical Performance in Thin-Film Solar Cells

Padmakumar, Govind; Criel, Matthias; Kashyap, Tanya; Saitta, Federica; Perez-Rodriguez, Paula; van Swaaij, René A. C. M. M.; Smets, Arno H. M.

DOI
10.1002/pip.70046

Publication date
2025

Document Version
Final published version

Published in
Progress in Photovoltaics: research and applications

Progress in Photovoltaics: Research and Applications

WILEY

PROGRESS IN PHOTOVOLTAICS

RESEARCH ARTICLE OPEN ACCESS

Superimposed Sacrificial Texturing to Enhance the Optical Performance in Thin-Film Solar Cells

Govind Padmakumar | Matthias Criel | Tanya Kashyap | Federica Saitta | Paula Perez-Rodriguez | René A. C. M. M. van Swaaij | Arno H. M. Smets

Photovoltaic Materials and Devices, Delft University of Technology, Delft, the Netherlands

Correspondence: Govind Padmakumar (g.padmakumar@tudelft.nl)

Received: 4 April 2025 | **Revised:** 30 September 2025 | **Accepted:** 21 November 2025

Keywords: diffused transmittance | glass texturing | nanocrystalline silicon | optical performance | reflectance | sacrificial texturing | solar cells | thin-film silicon

ABSTRACT

Techniques to facilitate excellent optical yield are required to manufacture high-performing solar cells. In thin-film solar cells, light scattering with the help of textured interfaces increases the absorption path length of photons and reduces the reflection of the photovoltaic active layer. These textures should also facilitate the growth of crack-free thin-film layers, ensuring high efficiency in multijunction devices. This work explores three texturing methods for glass that have the potential to be integrated into solar cells in a superstrate configuration. A detailed study of sacrificial texturing on glass using i-ZnO (SLT_{IZO}) and indium-doped tin oxide (SLT_{ITO}) is presented. The optical interaction of these textures is correlated to their root-mean-square (RMS) roughness (σ_{rms}). It is demonstrated that high optical scattering can be achieved for both SLT_{ITO} and SLT_{IZO} but at different σ_{rms} regimes. A novel texture with superimposed morphology, named superimposed sacrificial texturing (*SIT*), is created by combining SLT_{ITO} and SLT_{IZO} through sequential wet etching. The *SIT* exhibits exceptional transmission and light scattering properties. Nanocrystalline silicon (nc-Si:H) single-junction solar cells were fabricated in a superstrate configuration to investigate the impact of these textures on indirect bandgap thin-film solar cells. The efficiency of solar cells on *SIT* is nearly 0.57% and 1.52% (absolute) more than SLT_{ITO} and SLT_{IZO} solar cells, respectively. By superimposing two textures, solar cells can combine the advantages of enhanced optical performance with high-quality nc-Si:H material growth.

1 | Introduction

Progress in the conversion efficiencies of photovoltaic (PV) technologies requires a reduction of the fundamental optical, electrical and thermodynamic conversion loss mechanisms in solar cell devices. The introduction of textured interfaces in PV device architectures is a successful light management technique that improves the optical performance of solar cells. It enhances the PV-active absorption by enhancing the absorption path length of the light [1]. Texturing of interfaces is an integral process step in the manufacturing of various thin-film PV technologies, including CIGS, perovskites, amorphous-nanocrystalline silicon and wafer-based crystalline silicon (c-Si) PV technologies [2–4]. Thin-film silicon PV devices are often fabricated in a substrate or superstrate configuration. For thin-film PV modules, texturing the front window based on glass in a superstrate configuration or texturing the back reflector in a substrate configuration is typical to maximise light trapping.

The random surface texture and its surface features can be physically characterised by the root-mean-square roughness (σ_{rms}), lateral correlation length (L_{corr}) and aspect ratios (AR) [5]. Random textures exhibit a specific range of feature sizes that determine how the light interacts with the interface between two media (reflection, transmission and absorption). The nature of the incoherent scattering mechanisms and the

coherent refraction of light by these textured interfaces lies in their geometry and dimension in reference to the wavelength (λ) of the light [5]. The type of interaction is determined by the shape and size (S) of a surface feature in reference to the λ. For small sizes of surface features and roughness, incoherent Rayleigh scattering ($S < < \lambda$) and Mie scattering ($S \sim \lambda$) occur. In contrast, coherent refraction at an interface takes place at large 'macro'-sized features ($S \gg \lambda$) [6]. Because the textures present on the glass must maximise scattering over a broad spectral range (equivalent to the optical response of the thin-film absorber from the UV to the IR region), the shape and dimensions of the texture features should be present accordingly. Different textures, shapes, and sizes must coexist on a surface to maximise the optical gain. This article helps determine the type of texture and which texture sizes result in the highest transmission and light scattering, thereby increasing absorption in a solar cell.

A general challenge for integrating textured interfaces into thin-film PV devices is that texture features may induce inhomogeneities, defects, cracks or pinholes in the PV-active materials. This might deteriorate the film's electrical quality by enhancing Shockley-Read-Hall recombination of light-excited charge carriers. The relation between substrate roughness and the accompanying additional electrical losses is often reflected in reduced open-circuit voltage (V_{OC}) and fill factor (FF) of the solar cells as described in detail in [7–11]. This demonstrates that there is a delicate interplay between increasing optical yield using textured interfaces and preserving electrical performance [12–16].

Glass is an amorphous solid with a random network of silicon and oxygen atoms [17]. The absence of both well-defined lattice structure and a suitable etching process makes glass texturing extremely challenging, especially for large-area applications. Methods such as photolithography [18, 19] and wet etching of sacrificial aluminium [20] or sacrificial transparent conductive oxide (TCO) layers [21, 22] on top of glass substrates are commonly employed to create craters on glass. Photolithography is an expensive and time-intensive process, especially for large-area processing [23]. For wet chemical etching using a sacrificial layer, a polycrystalline TCO layer like indium-doped tin oxide (ITO) [22], aluminium-doped zinc oxide (AZO) [24] or gallium-doped zinc oxide (GZO) [25] acts as a 'leaking' mask that is partly or wholly removed during a chemical wet-etching process. The etching solution penetrates the easiest through pinholes and pores around grain boundaries in the TCO material [26]. As the sacrificial TCO layer is dissolved, the glass is inhomogeneously etched, resulting in a random texture on the surface. In previous studies, ITO has often been used as a sacrificial TCO layer to add microscale texture and AZO as a sacrificial layer to impart nanoscale textures to glass.

To demonstrate the potential of multiscale features coexisting on glass, a modulated surface texturing (MST) concept was implemented by Isabella et al. for substrate configuration. The MST combined etched glass ($\sigma_{rms} = 200$ nm) with AZO-induced sacrificial textures ($\sigma_{rms} = 82$ nm) [5]. Later, the MST concept was extended to nanotextures generated with partially etched AZO in a superstrate configuration solar cell device by Tan et al. and Yang et al. [8, 22, 26]. But these methods had the drawback of parasitic UV light absorption by the retained AZO or ZnO when implemented in a superstrate configuration. This report presents an extensive sample-size study of nanoscale and microscale textures for the first time, aiming to determine the design rules for optimal modulated texturing conditions. A novel texturing method is required to address these issues for implementing the MST concept in superstrate thin-film devices. In solar cells, nanocrystalline silicon is an ideal material to illustrate the performance of textures because it behaves as an indirect bandgap material in the spectral range of 800–1100 nm and requires light trapping concepts to enhance the absorption in this wavelength range [27, 28].

This work focuses on undoped zinc oxide (i-ZnO) as a novel sacrificial TCO material for creating small-sized craters on glass. We also explore in detail the conventional method of using ITO as a TCO sacrificial layer to make large-scale textures. In addition, multiple-step etching of the glass is identified as a route to create modulated surface textures at the glass surface. The properties and thickness of the sacrificial TCO layers are varied to make an extensive range of surface features and texture sizes. Through a comprehensive study of this sample set, the relation between light scattering, quantified in terms of diffused transmission (T_D) and σ_{rms}, has been revealed. This empirical relation serves as a guideline for developing superimposed textured surfaces (SITs) with a broad spectral range of light scattering. The optical performance of textured glass substrates in solar cells is demonstrated using hydrogenated nanocrystalline silicon (nc-Si:H) single-junction PV devices. The nc-Si:H single-junction solar cell devices are fabricated in a superstrate configuration to compare the impact of all three developed textures on optical and electrical device performance. An identical solar cell architecture is fabricated on flat glass to observe the optical response when light scattering is negligible. The thin-film nc-Si:H absorber layers adopt the morphology of the textured glass when they are processed in a superstrate configuration. It is demonstrated that exceptional optical performance can be combined with good electrical performance using *SIT*.

2 | Materials and Methods

Corning XG glass, 0.7 mm thick with $\sigma_{rms} < 10$ nm [29, 30], is used as a substrate throughout this study to develop textures. In the study presented here, two different TCO masking materials have been selected, namely, ITO and i-ZnO. Three different texturing approaches are presented in this work: (i) ITO sacrificial layer texturing (SLT_{ITO}), (ii) i-ZnO sacrificial layer texturing (SLT_{IZO}) and (iii) superimposed sacrificial texturing (*SIT*), which uses both ITO and i-ZnO for texturing. Varying several processing parameters alters the crystallinity (χ_c), density and thickness of these sacrificial TCO layers, resulting in the creation of textures with different shapes and dimensions [31, 32].

2.1 | ITO Sacrificial Layer Texturing—SLT_{ITO}

SLT_{ITO} is developed using ITO deposited on glass. A flowchart of the processing method is presented in Figure 1. The first five

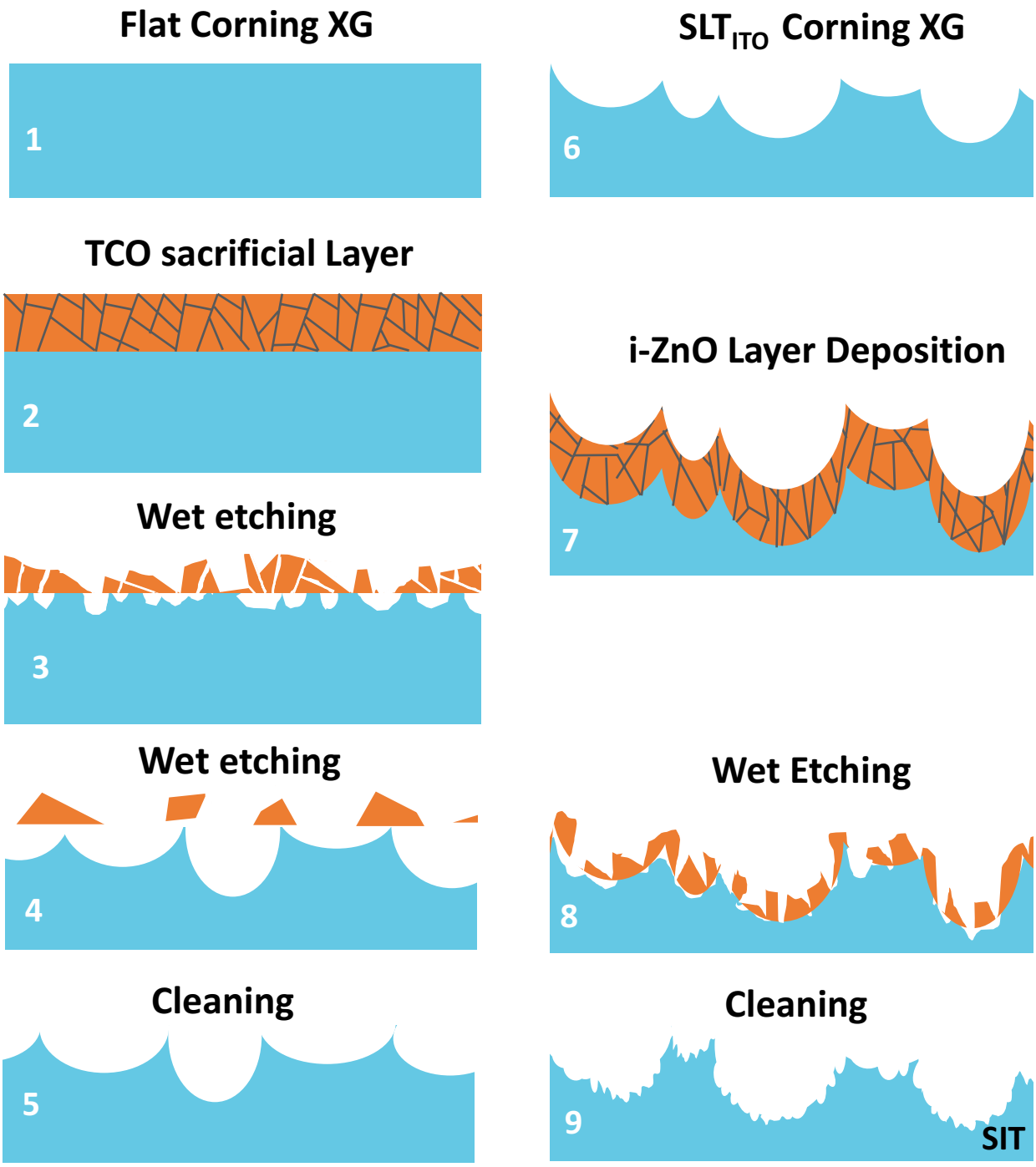

FIGURE 1 | Flowchart of the sacrificial texturing approach. Steps 1–5 are the development of SLT_{ITO} or SLT_{IZO} depending on the TCO layer. Steps 6–9 are representations of the superposition of SLT_{IZO} over SLT_{ITO}. Processing Steps 1–9 are referenced in the text. Step 3 illustrates an intermediate phase that occurs shortly after the etchant has reached the glass, and Step 4 shows the result after the required time has elapsed, resulting in craters and the complete removal of the sacrificial layer.

steps represent SLT_{ITO} texturing. In Step 1, Corning XG glass is cleaned in ultrasonic baths of acetone and 2-propanol for 10 min each. During Step 2, ITO is deposited as a sacrificial TCO layer using magnetron sputtering at elevated temperatures. The properties of the deposited layer are controlled by varying the physical parameters of power, pressure and temperature [33, 34]. In subsequent Steps 3 and 4, the layer deposited on the flat glass is wet-etched. Step 3 is the phase in which the TCO is being etched up to the moment the etchant reaches the glass–TCO interface. Step 4 corresponds to the phase in which both TCO and glass are being etched. During Steps 3 and 4, the TCO deposited over the glass is removed and dissolved into the bath, and the textures referred to as SLT_{ITO} are visible on the glass surface. The etchant solution used in this study is HF (40%):H_2O_2 (31%):H_2O in the ratio 1:2:10. After Step 4, the textured samples are cleaned by dipping in HNO_3 (69.9%) for 3 min (Step 5). This step removes any possible remaining ITO residues.

2.1.1 | Design of Experiment

To vary the properties of the ITO layer, the deposition conditions are varied over different combinations of RF power, temperature and thickness. The deposition temperature ranges between 200°C and 300°C. Deposition power density varies between 1.35 and 2.45 W/cm2. The thickness of the deposited ITO layer ranged from 150 to 400 nm. In this specified range of deposition conditions, 35 different conditions have been explored to create different SLT_{ITO} textures.

2.2 | i-ZnO Sacrificial Layer Texturing—SLT_{IZO}

A similar approach as in Section 2.1 is employed for SLT_{IZO}. The flowchart of the processing method is given in Figure 1, Steps 1–5. During Step 2, an i-ZnO layer is deposited as a sacrificial layer using magnetron sputtering. These layers are subsequently wet-etched using a HF (40%) solution and HNO_3 (69.9%) solution in a 1:8 ratio in Steps 3 and 4. The residual TCO is cleaned by dipping in HNO_3 (69.9%) for 3 min in Step 5.

2.2.1 | Design of Experiment

The i-ZnO layer deposition temperature varies between 25°C and 400°C. The deposition power density varies between 0.5 and 4.0 W/cm2. The resulting thickness of i-ZnO is between 120 and 300 nm. Twenty-six conditions were explored within this specified range of deposition conditions.

2.3 | Superimposed Sacrificial Texturing—*SIT*

SIT is developed by superimposing SLT_{IZO} on SLT_{ITO} using two cycles (Steps 1–5 and Step 6–10) of sacrificial etching as shown in Figure 1 in sequence. For this, the deposition conditions resulting in the highest diffused transmission SLT_{ITO} and SLT_{IZO} (will be discussed in Section 3.2 were utilised to make *SIT*. In step 2 (first cycle), SLT_{ITO} sacrificial layer of 360-nm thickness is deposited at 230°C temperature and 2.1 W/cm2 power density on cleaned glass. This is subsequently etched as mentioned in Section 2.1 to make craters of SLT_{ITO} (Steps 3–5). In Step 7, during the second cycle, a 140-nm-thick layer of i-ZnO is deposited at 200°C, 4 W/cm2 and 2.6-mBar pressure on the textured side of SLT_{ITO}. This is followed by wet etching (Step 8) of the i-ZnO layer by similar processes explained in Section 2.2. The residual TCO layers were removed, and samples were cleaned by dipping in HNO_3 (69.9%) for 3 min (Step 9).

The textures made and their summary of characterisation techniques are given as a flow chart in Figure 2. The characterisation methods are detailed in the upcoming sections.

2.4 | Characterisation of Textures

Atomic force microscopy (AFM) is carried out to examine the surface morphology of developed textures using a Bruker AFM FastScan in the FastScan closed-loop scanner head modus. Scanning sizes of a 16 μm × 16 μm and a 30 μm × 30 μm were chosen for analysing the differently sized textures. In cases when small-area scans (16 μm × 16 μm) were not enough to capture all typical feature sizes and their fractal nature, larger area scans were opted for (30 μm × 30 μm). The surface parameters σ_{rms}, power spectral density (PSD) and slope distribution were extracted from the AFM data using the NanoScope Analysis software from Bruker. PSD is used to represent the morphology of textures quantitatively. PSD of the height variation on the surface is a spatial frequency representation of the surface based on a discrete two-dimensional Fourier transform of the height–height correlation function [35, 36]. NanoScope analyses the surface slopes based on the normalised occurrence distribution of angles subtended by surface vectors with the vertical plane. Further, the textures were analysed for their increase in effective surface area, which is defined as the ratio (in percentage) of the real surface area of the texture to the projected area. The effective surface area analysis is completed using Gwyddion software (Version 2.63). In addition, the surface textures have been analysed using scanning electron microscopy (SEM) with a Hitachi Regulus 8230 at an acceleration voltage of 1.5 kV.

To characterise textures optically, the transmission of all glass samples was measured with probing light on the flat side as shown in Figure 3a. Optical transmission measurements were performed using a LAMBDA 1050+ UV/Vis/NIR Spectrophotometer equipped with a 150 mm InGaAs integrating sphere from PerkinElmer. The angular intensity distribution (AID) of transmitted light was examined using the 180-mm automated reflectance/transmittance analyser (ARTA22) accessory on a LAMBDA 950 PerkinElmer unit. Measurement methods of AID for transparent objects can be found in [37, 38]. The percentage of light transmitted in any direction other than normal is quantified as diffused transmittance (T_D). T_D values at different

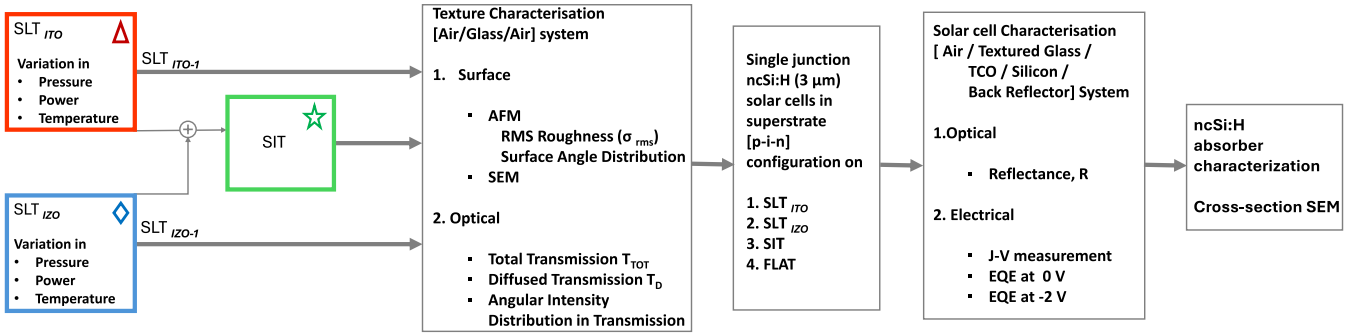

FIGURE 2 | Flow chart representing the design of the experiment and characterisation steps.

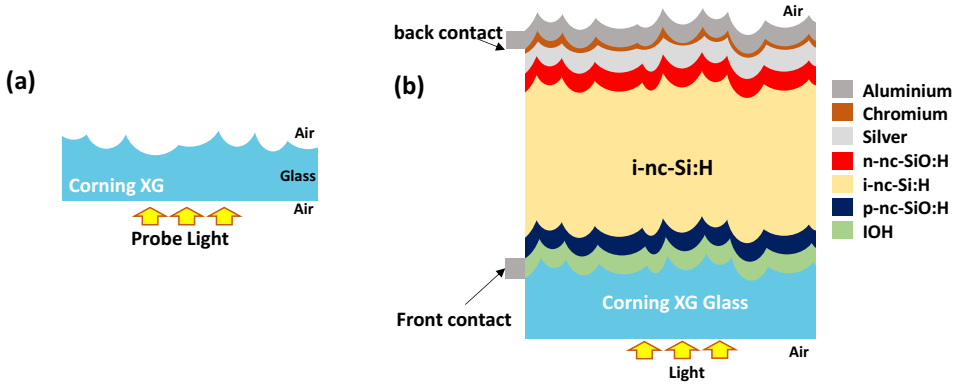

FIGURE 3 | (a) Representation of air/textured glass/air system probed from flat side. (b) Schematic diagram of a 5 mm×5 mm solar cell made on a glass superstrate configuration. Probing direction is also shown for the air/textured glass/IOH/ silicon solar cell/back reflector system.

wavelengths were considered the prime metric for quantifying the optical scattering performance of the textured glass in this work.

2.5 | Solar Cells on Textures

Finally, the impact of textures on the optical and electrical performance of solar cells, as well as their effect on absorber crystal growth, was investigated. Solar cells were made on selected substrates of SLT_{ITO}, SLT_{IZO}, *SIT* and also on nontextured Corning XG glass (FLAT) for reference. Hydrogenated nanocrystalline silicon (nc-Si:H) single p-i-n junction solar cells were made in a superstrate configuration with an area of 5 mm×5 mm. The solar cell architecture is shown in Figure 3b.

The solar cells have hydrogenated indium oxide (IOH) as the front electrode TCO. IOH is RF magnetron sputtered from a ceramic indium oxide (In_2O_3) target in $Ar/O_2/H_2O$ mixtures. The introduction of water vapour prevents crystalline growth of IOH, and the resulting IOH deposited at room temperature is amorphous [39, 40]. This choice of IOH is made because it is flat by nature and omits the possibility of any added roughness and light scattering by TCO grains [41, 42]. The silicon alloy deposition was done on a plasma-enhanced chemical vapour deposition (PECVD) multichamber tool with dedicated processing chambers for the boron-doped nc-Si:H oxide p-layer (B-doped p-nc-SiO_x:H), intrinsic nc-Si:H (i-nc-Si:H) and phosphorus-doped nc-Si:H oxide n-layer (n-nc-SiO_x:H). The B-doped nc-SiO_x:H layer (16 nm thick) and p-doped nc-SiO_x:H n-layer (20 nm thick) were deposited using radiofrequency (13.8 MHz) in the PECVD tool at 180°C substrate temperature and using B_2H_6 and PH_3 as dopant gasses, respectively. The i-nc-Si:H absorber layer was deposited at very high frequency (40.68 MHz) at 170°C substrate and deposition rate of 4.9 Å/s. The solar cells have a back reflector consisting of sputtered i-ZnO (60 nm) and an evaporated silver (300 nm) layer. The front contact is an aluminium strip with a thickness of 500 nm, and the back contact consists of chromium (30 nm) and aluminium (500 nm). The solar cell area is defined by 5 mm×5 mm squares. This results in a solar cell structure of IOH (150 nm)/p-nc-SiO:H (16 nm)/i-nc-Si:H (3000 nm)/n-nc-SiO:H (20 nm)/i-ZnO (60 nm)/Ag (300 nm). No external front anti-reflective coatings were applied to the solar cells presented in this study.

The specific deposition parameters are included in Table 1. The deposition rates, refractive indices (n), and extinction coefficients (k) of the mentioned layers (except the nc-Si:H absorber) were measured using spectroscopic ellipsometry, and the data are included in the supplement. The deposition parameter optimisation of the 3200-nm-thick nc-Si:H bulk photoactive layer is conducted on microtextured glass, with χ_c as the chosen parameter. The deposition conditions are optimised to attain a χ_c between 55% and 65% to ensure the use of high-quality material [43–45]. The deposition rate of nc-Si:H was determined with SEM cross-section imaging. The n and k values of nc-Si:H are determined with the effective medium approximation method.

The V_{OC} and FF of solar cells were measured by a WACOM-class AAA xenon-halogen dual lamp continuous AM1.5G spectral simulator at 25°C. The short-circuit current density (J_{sc}) values were calculated based on the external quantum efficiency (EQE) measurement of solar cells ($J_{sc,EQE}$). This helps to prevent the effect of any mismatch between the solar simulator spectrum and the AM1.5 spectrum. Also, it eliminates any overestimation of current caused by errors in estimating the active cell area in small-area solar cells. EQE measurement is conducted at a short-circuit condition of 0 V and a reverse bias condition of –2 V. The total reflection of the solar cell is also recorded, with the help of LAMBDA 1050+ UV/Vis/NIR Spectrophotometer with a 150-mm InGaAs integrating sphere from PerkinElmer.

3 | Results and Discussion

Sacrificial layers of TCOs, each different from the others, were deposited on flat glass and etched to develop random textures on the glass using the sacrificial method successfully. When observed under SEM, the i-ZnO exhibits a columnar crystal growth, whereas ITO exhibits bulky growth for its crystals, as shown in Figure 4. Wet etching of ITO and i-ZnO sacrificial layers deposited by varying power, pressure and temperature produced surface textures over a wide range of σ_{rms} values. In the upcoming sections, the discussions will be based on two optical systems: (i) air/glass/air and (ii) air/glass/IOH/nc-Si:H solar cell/silver. The former system provides insights into the physical

TABLE 1 | Deposition conditions of different layers in the solar cell.

Layer	SiH_4 (sccm)	H_2 (sccm)	Dopant gas (sccm)	CO_2 (sccm)	Pressure (mBar)	Power (W/cm_2)	Electrode gap (mm)	Deposition rate (Å/s)
p-nc-SiO_X	0.8	170	10 0.02% B_2H_6 in H_2	1.2	2.2	0.12	13	0.33
i-nc-Si:H (seed)	1.1	120	—	—	4	0.4	13	2.3
i-nc-Si:H (bulk)	3.2	120	—	—	4	0.4	13	4.9
n-nc-SiO_X	1	170	2 2% PH_3 in H_2	1.6	1.5	0.11	21	0.16
TCO	Ar (sccm)		H_2O partial pressure		Pressure (mBar)	Power	Substrate temp. (°C)	Deposition rate (Å/s)
IOH (front electrode)	50	—	0.06	—	5.7	1.5	27	0.98
i-ZnO (back reflector)	20	—	—		2.6	2.0	130	0.87

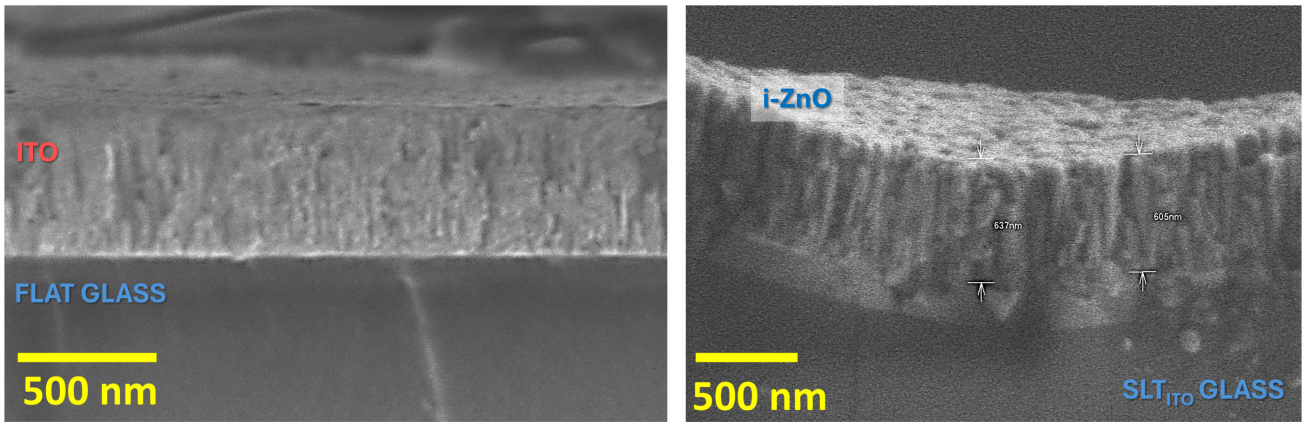

FIGURE 4 | ITO and i-ZnO crystal structure observed with SEM on flat glass. ITO demonstrates a bulky growth on glass while i-ZnO has a columnar growth of the crystals.

and optical behaviour of developed textures, while the latter offers conclusions on their impact when employed in a solar cell. The optical properties of textures in one system are not one-to-one translatable to the other because the Fresnel reflection and transmission coefficients differ. Additionally, system (ii) exhibits multiple reflections at the interfaces.

3.1 | Physical Characterisation of SLT_{ITO}, SLT_{IZO} and *SIT*

The shape of craters made using the sacrificial texturing method was observed with SEM and AFM. Data of SLT_{ITO}, SLT_{IZO} and *SIT* samples are shown in Figures 5–7, respectively. The image suggests that SLT_{ITO} possesses sharp boundaries with a polygonal shape on the glass surface, compared with SLT_{IZO}, which has more circular borders. Another interesting visual observation is that SLT_{ITO} possesses a larger fraction of hexagon-shaped craters, whereas SLT_{IZO} has a larger fraction of tetragon- and pentagon-shaped craters. *SIT* was successfully made by wet-etching i-ZnO layer deposited on SLT_{ITO} texture. Upon executing this sequential etching step on SLT_{ITO}, a superimposed version of craters is identified on the glass surface as shown in Figure 7. This is made possible as the sputtered i-ZnO films have more frequent boundaries compared with ITO to act as a 'leaking mask'. This columnar structure of i-ZnO allows

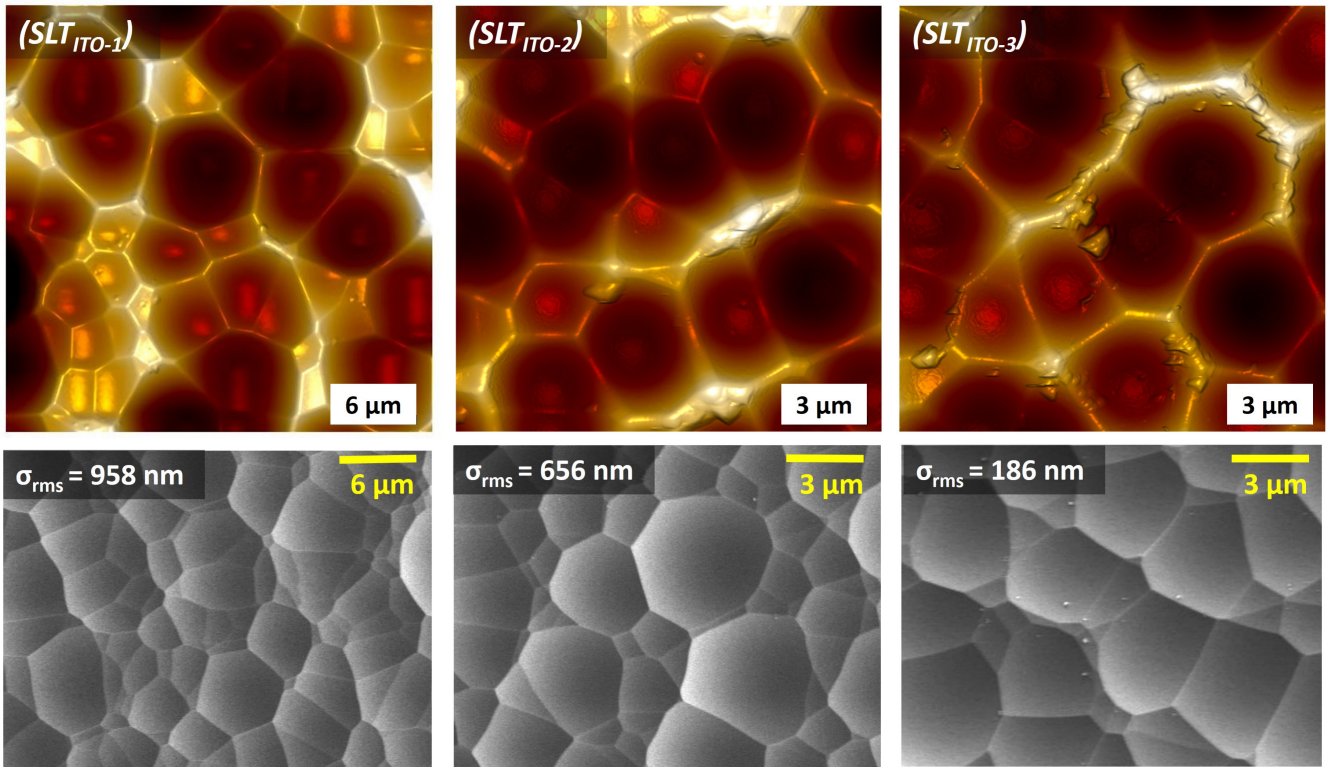

FIGURE 5 | AFM images (top row) and SEM image (bottom) of SLT_{ITO} samples. From left to right, the samples have a decrease in σ_{rms}. N.B. Area of SLT_{ITO-2} and SLT_{ITO-3} is 16µm×16µm and SLT_{ITO-1} is a 30µm×30µm.

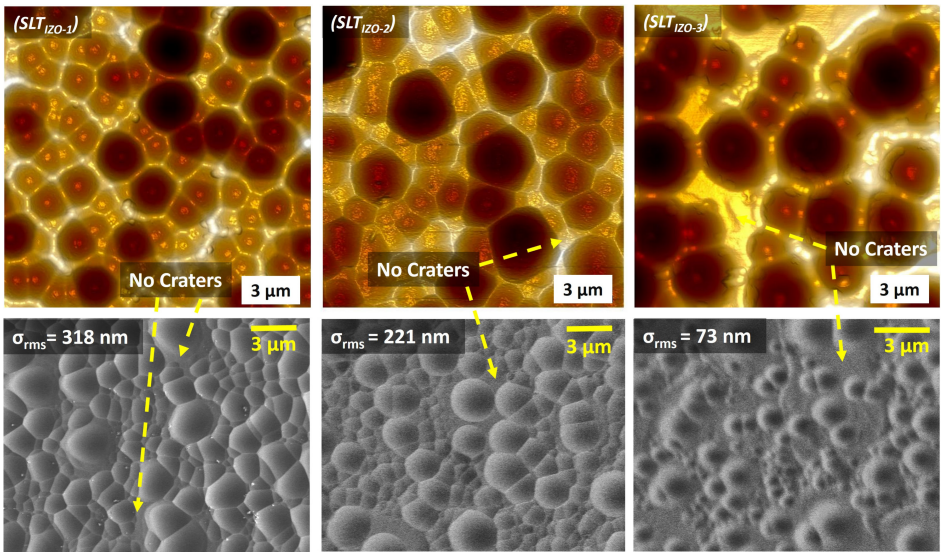

FIGURE 6 | AFM images of SLT_{IZO} samples (top row) and SEM image of SLT_{IZO} samples. From left to right, the samples have a decrease in σ_{rms} and an increase in flat regions.

multiple paths for the etchant to reach the glass surface and create craters within the large craters of SLT_{ITO}. This phenomenon occurs uniformly across the entire surface. Multiple leak paths for the chemical also result in a quicker removal of the deposited i-ZnO mask (in comparison with ITO) from the surface, which also limits the depth of SLT_{IZO} craters (compared with SLT_{ITO}).

The surface profiles extracted from AFM data of the samples SLT_{ITO-1}, SLT_{IZO-1}, *SIT* are given in Figure 8a–c, respectively. To visualise the signature shape of craters in three dimensions (3D), an isometric view (15µm×15µm) of surfaces is shown in the inset. The isometric view for SLT_{ITO} (Figure 8a) shows an 'inverted U' shape, suggesting that it resembles spherical sectors. The surface craters of SLT_{IZO} (Figure 8b) show an 'inverted V' shape at the edge, suggesting the dips resemble inverted cones. While adding the surface morphologies, SLT_{ITO} accommodates small cones of SLT_{IZO} in its wide spherical craters to form *SIT* (Figure 8c, inset). Interestingly, the *SIT* maintains the

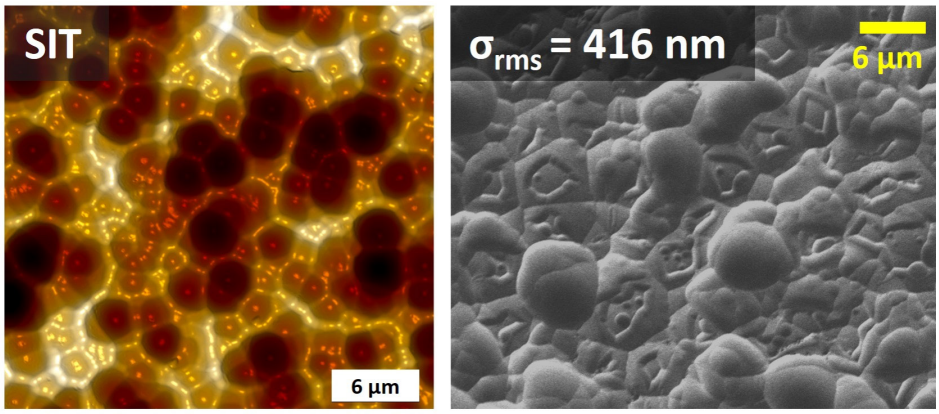

FIGURE 7 | AFM data (left) and SEM images (right) of *SIT*.

polygonal-shaped borders inherited from SLT_{ITO} on its surface. The amplitude of the extracted profile of the SLT_{IZO} sample is 0.5µm, and that of SLT_{ITO} is 2µm. The second etching step in *SIT* fabrication reduces the amplitude of *SIT* to 1.3µm from the high amplitude of SLT_{ITO}. After etching, the textures show an increase in effective surface area by 8.0% for SLT_{ITO}, 2.5% for SLT_{IZO} and 6.8% for *SIT* when compared with FLAT.

3.1.1 | Slope Distribution of the Surfaces

Slope analysis of the textures obtained from their respective AFM scans is given in Figure 9. The conical shape of SLT_{IZO} results in a concentrated slope distribution in the range 0° to 38° ($maximum \approx 7°$) in contrast to spherical sector-like SLT_{ITO} with wider angle distribution from 0° to 55° ($maximum \approx 16°$). Upon superimposition, the slope distribution of *SIT* resembles the shape of the slope distribution of SLT_{ITO}, but at the same time shows a shift in peak. The range of surface slope for *SIT* is determined by the largest sized textures (of SLT_{ITO}), whereas covering the whole area by small conical features (of SLT_{IZO}) shifts the peak occurrence value to the left ($maximum \approx 12°$). The texture regions contributing to shallow angles (taken as 12° here) are depicted in Figure 10. The wider shallow angle region (greyscale) at crater boundaries of *SIT* compared with SLT_{ITO} implies that the sharp peaks of SLT_{ITO} are marginally rounded in *SIT* during the second etching step.

3.1.2 | PSD Analysis of the Textures

Figure 11 is a PSD analysis of three surfaces SLT_{ITO-1}, SLT_{IZO-1} and *SIT*. The PSD of a texture at low frequencies (Zone 1) characterises the features with large lateral and vertical dimensions. The high frequency (Zone 2) represents small dimensions in the textures. The influence of feature sizes on light scattering has been widely discussed with PSD as a tool [5, 46]. It is ideal to have features from both Zones 1 and 2 in a solar cell, allowing light scattering to occur across a broad wavelength range. Spectrum scattering by the discussed features in Zone 1 is coherent scattering, which can be understood using ray optics models, whereas Zone 2 features (where $S \leq \lambda$) can be understood with Mie scattering and incoherent diffraction [5, 47]. The highest occurrence for large features is for SLT_{ITO}, and the lowest is for SLT_{IZO}. This implies that the scattering mechanism of SLT_{ITO} is predominantly coherent refraction. The small features occur the most in *SIT*, followed by SLT_{IZO}. The fact that *SIT* has most small-scale features is highly likely a combined result of small textures inherited from SLT_{IZO} and pre-existing crater boundaries of SLT_{ITO}. This also implies that *SIT* is not a perfect superposition of SLT_{IZO} and SLT_{ITO}. These observations predict that *SIT* can be active in interacting with light over the wide range of spectrum from 300 to 1100 nm.

3.1.3 | Roughness of the Textures

Due to the self-affinity of the random textured surfaces, general fractal scaling laws show that the scan size needs to be much larger than the typical feature sizes ($L \gg S$) to accurately determine L_{corr} [48]. The AFM scan size is smaller than the required size for features considered in this paper. Therefore, in the remainder of this article, we will plot the optical properties as a function of σ_{rms} to demonstrate the empirical relation between parameters.

For SLT_{ITO}, the obtained σ_{rms} value ranges from 186 to 1124 nm. SEM images (Figure 5) imply that the cause of the increase of σ_{rms} for SLT_{ITO} is a result of the increased crater depths. For SLT_{IZO}, the attained σ_{rms} value ranges between 73 and 336 nm. Also, SLT_{IZO} can result in flat regions on the glass, which can reduce its σ_{rms} (Figure 6, SLT_{IZO-3}). A wide range of σ_{rms} values across SLT_{IZO} samples explicitly shows that the variation in i-ZnO's deposition conditions can be used to tune the texture properties. This is similar to observations on nanoscale sacrificial texturing using AZO layers [21, 22]. The σ_{rms} of *SIT* determined from the 2D AFM scan area 30µm×30µm is 416 nm. This σ_{rms} is intermediate to the roughness of its two constituent morphologies.

3.2 | Diffused Transmission of SLT_{ITO}, SLT_{IZO} and *SIT*

3.2.1 | T_D Data of SLT_{ITO}

In Figure 12, T_D for each SLT_{ITO} sample is shown as the percentage of total transmitted light. The diffusivity of transmitted light gradually increases with σ_{rms} for $\sigma_{rms} < 500$ nm. For

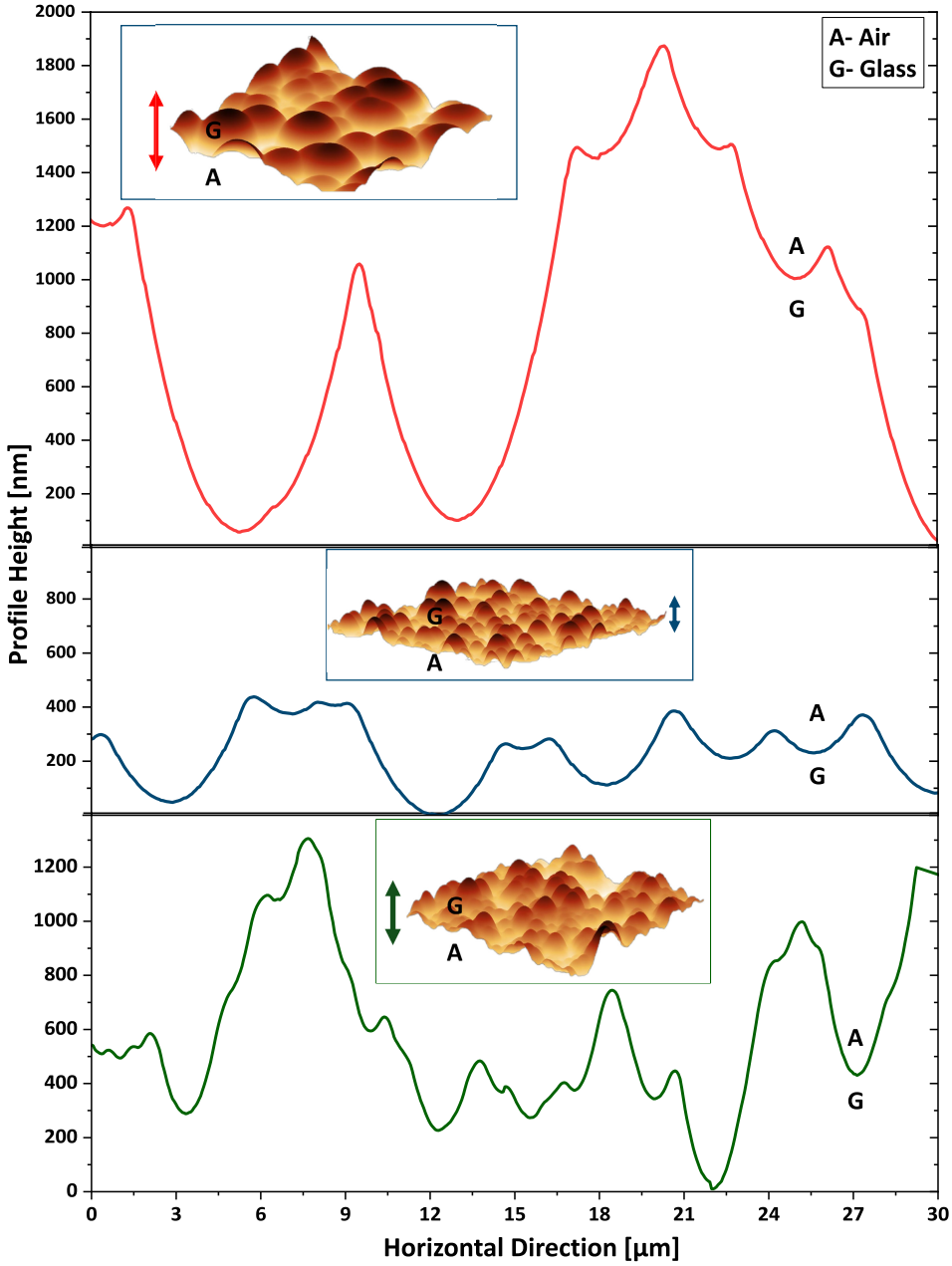

FIGURE 8 | Surface profile over 30-µm length (all graphs in the same scale) of *top*: SLT_{ITO-1} sample, *middle*: SLT_{IZO-1} sample and *bottom*: *SIT* sample and their isometric views (inset). The surface is the glass (G)/air (A) interface, with media as indicated for each image. N.B. The inset images are flipped vertically to display their features.

$500\,\text{nm} < \sigma_{rms} < 800\,\text{nm}$, there is a steeper increase in T_D. T_D saturates for $\sigma_{rms} > 950\,\text{nm}$. Three samples of SLT_{ITO}, namely, SLT_{ITO-1}, SLT_{ITO-2} and SLT_{ITO-3}, are marked on the plot T_D versus σ_{rms}. The mechanism of scattering in SLT_{ITO} is refractive—governed by the refractive properties of the medium at the interface. For this reason, deep textures like SLT_{ITO-1} effectively scatter light, whereas for SLT_{ITO-3} with shallow craters, the diffusivity is limited.

The observed T_D for SLT_{ITO-1} at $\lambda = 400, 600, 800, 1000\,\text{nm}$ are 84%, 80%, 79% and 78%, respectively. SLT_{ITO-1} was made from a 360-nm-thick sputtered ITO sacrificial layer deposited at a temperature of 230°C, power density of 2.1 W/cm2, chamber pressure 16 mBar and an argon flow of 45 sccm.

3.2.2 | T_D Data of SLT_{IZO}

T_D values for each SLT_{IZO} sample were recorded as the percentage of total transmitted light in Figure 12. The increase in T_D is monotonous with the increase in σ_{rms}. Three samples of SLT_{IZO}, namely, SLT_{IZO-1}, SLT_{IZO-2} and SLT_{IZO-3} are highlighted in the data plot in Figure 12. The scattering mechanism in SLT_{IZO} is mainly incoherent diffraction, which is related to the *S* of texture. The best scatterers in the set of SLT_{IZO} samples are glass samples with uniformly distributed and well-developed craters, similar to those in SLT_{IZO-1}. The small σ_{rms} samples like (SLT_{IZO-3}) have intermediate regions without any craters (as observed in Figure 6). This explains the limited scattering ability of SLT_{IZO-3} over all λ.

In this experiment, the highest value of T_D is attained at $\sigma_{rms} = 318$ nm. This sample, SLT_{IZO-1}, was etched from the glass with a 140-nm-thick layer of i-ZnO deposited at 200°C, 4W/cm2, 2.6-mBar pressure and 20-sccm argon flow. The T_D values are 75%, 71%, 67% and 55% at $\lambda = 400, 600, 800$ and 1000 nm, respectively.

3.2.3 | T_D of *SIT*

The data point at $\sigma_{rms} = 416$ nm in Figure 12 (the green star) represents T_D of *SIT*. The processing conditions of the ITO layer and the i-ZnO layer in *SIT* correspond to those of SLT_{ITO-1} and SLT_{IZO-1}, respectively. *SIT* displays a T_D higher than all SLT_{IZO}s but lower than the best SLT_{ITO}.

Figure 12 demonstrates that at $\lambda = 400, 600, 800$ and 1000 nm, *SIT* diffuses 77%, 73%, 70% and 66% of transmitted light, respectively. *SIT* at relatively small σ_{rms} shows a high T_D which is nearly equal to T_D of SLT_{ITO-1}. For λ =400 and 600, the data point of *SIT* appears similar to an extrapolated point of SLT_{IZO}, suggesting a scattering mechanism similar to SLT_{IZO}. For $\lambda > 600$, *SIT* shows a minor drop in T_D—a behaviour similar to SLT_{ITO}s.

In the upcoming sections, names SLT_{ITO} and SLT_{IZO} refer to the sample with the highest observed T_D of the set, that is, SLT_{ITO-1} and SLT_{IZO-1}, respectively.

3.3 | AID of SLT_{ITO}, SLT_{IZO} and *SIT*

AID of SLT_{ITO}, SLT_{IZO} and *SIT* for four different λ are compared in Figure 13. SLT_{ITO} scatters the light over wider angles for all λ compared with SLT_{IZO} and *SIT*. AID of SLT_{ITO} is the highest for near infrared ($\lambda = 850$ nm) and red ($\lambda = 700$ nm), where the wavelength is comparable with σ_{rms} of SLT_{ITO}. SLT_{IZO} shows the highest AID for $\lambda = 400$ nm, where λ is comparable with its σ_{rms}. The scattered light intensity for $\lambda = 850$ nm steeply drops beyond 40° angles and reaches zero at 65°. The

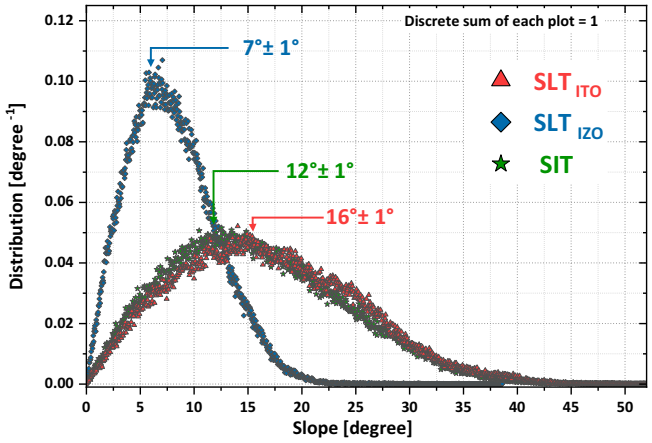

FIGURE 9 | Surface normal distribution curves of SLT_{ITO}, SLT_{IZO} and *SIT* in terms of angle. The occurrence value is normalised such that the total of each curve adds up to 1. Different angle ranges are identified in the supplementary data.

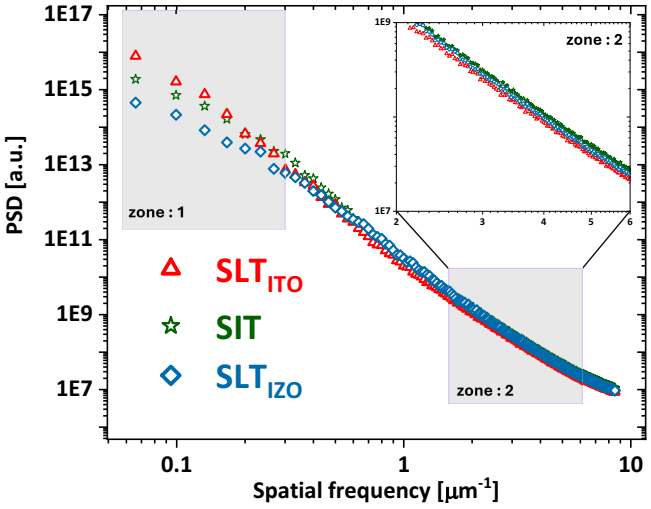

FIGURE 11 | PSD function versus spatial frequency of SLT_{ITO-1}, SLT_{IZO-1} and *SIT*. Zone 1 corresponds to large feature sizes, and Zone 2 corresponds to small feature sizes.

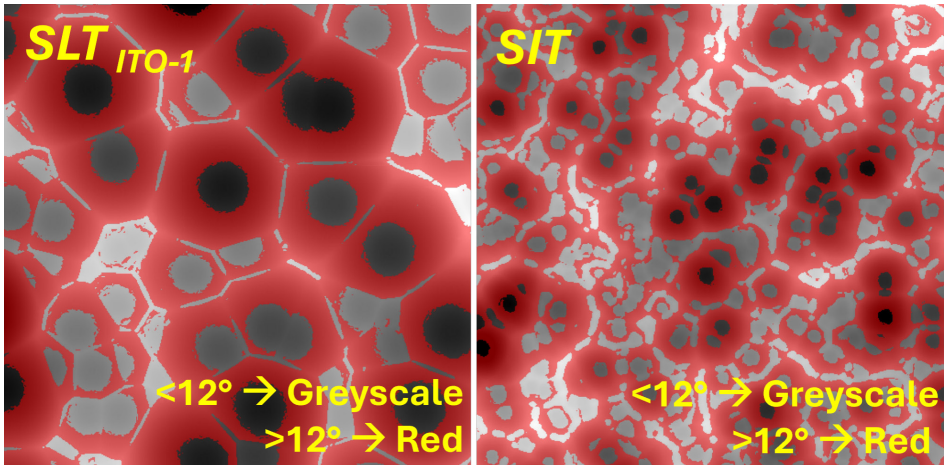

FIGURE 10 | Surface angle distribution of SLT_{ITO} and *SIT*. The occurrence of angles less than and greater than 13° is specified. The areas of both AFM scans are 30µm×30µm.

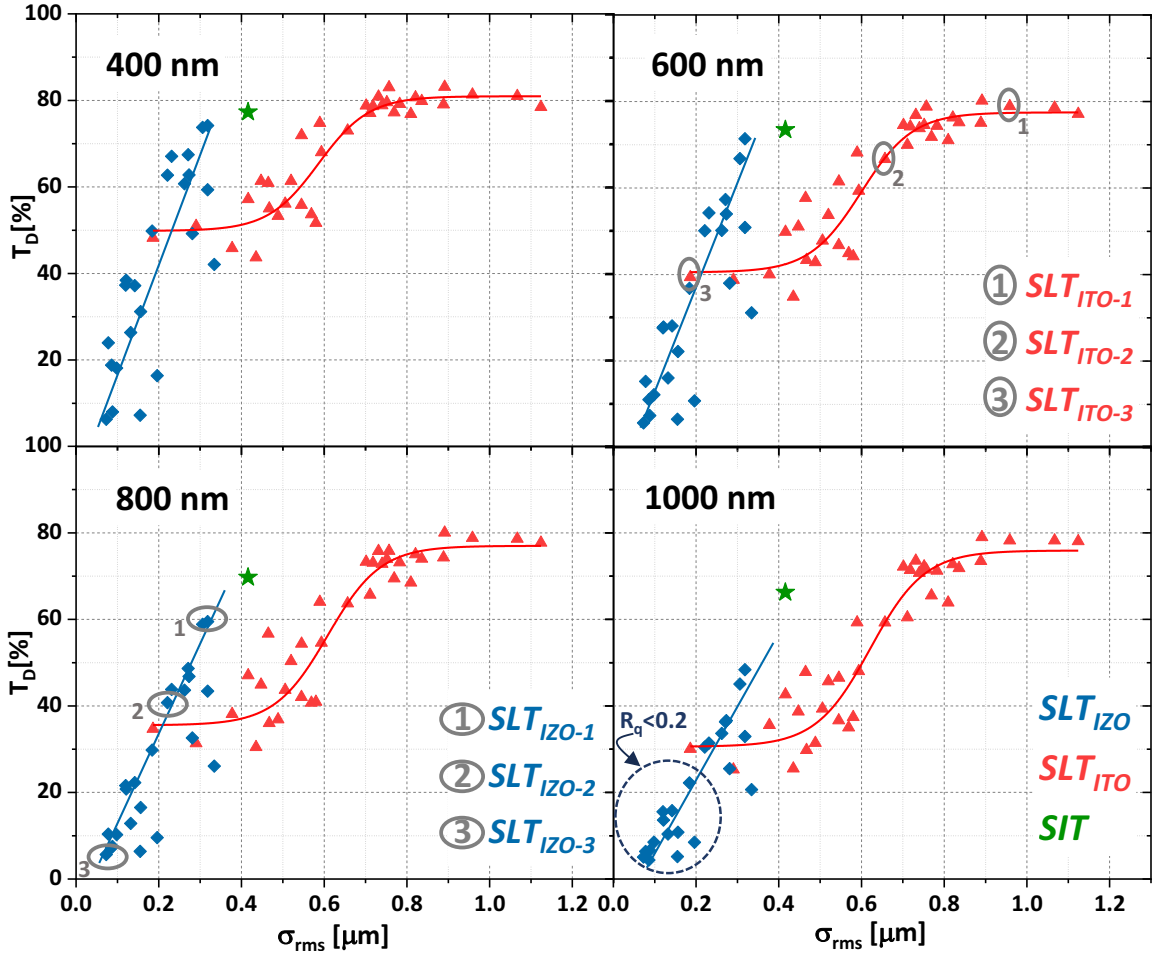

FIGURE 12 | Diffused transmittance values in percentage of different sacrificial textures, SLT_{ITO} (red and triangle), SLT_{IZO} (blue and diamond) and *SIT* (green and star) at wavelengths 400, 600, 800 and 1000 nm. The lines are a guide to the eye.

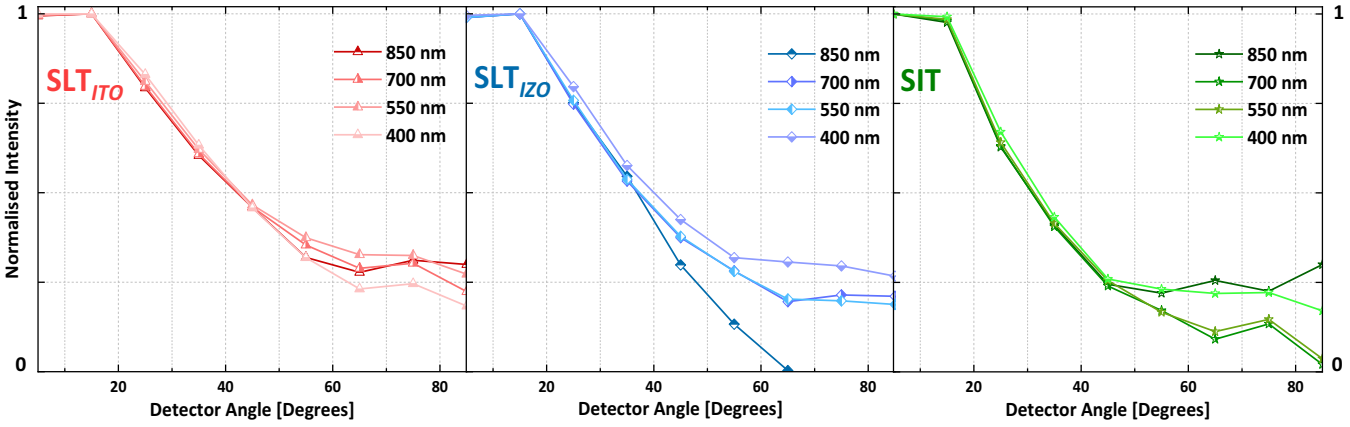

FIGURE 13 | Angle-dependent transmission properties of SLT_{ITO}, SLT_{IZO} and *SIT*: (a) Normalised intensity as a function of scattering angles (5°–85°). Normalisation is performed with respect to the maximum intensity. N.B. To interpret intensity normalised AID graphs of a specific texture at a particular wavelength, use the corresponding T_D (%) values of that texture at that wavelength in Figure 14.

diffractive scattering nature of SLT_{IZO} is the reason for the quick drop of T_D for $\lambda = 850$ nm. This same effect is also observed in Figure 12 in the form of accumulated data points for $\lambda = 800$ and 1000 nm at $\sigma_{rms} < 0.2$ (highlighted with circle in the graph). *SIT* exhibits an intermediate AID of its constituent textures. The diffused transmittance trends in Figure 14 also demonstrate the same. *SIT* exhibits good angular scattering for $\lambda = 400$ and 850 nm, presumably because the constituent features of SLT_{ITO} and SLT_{IZO} are closest comparable with these values.

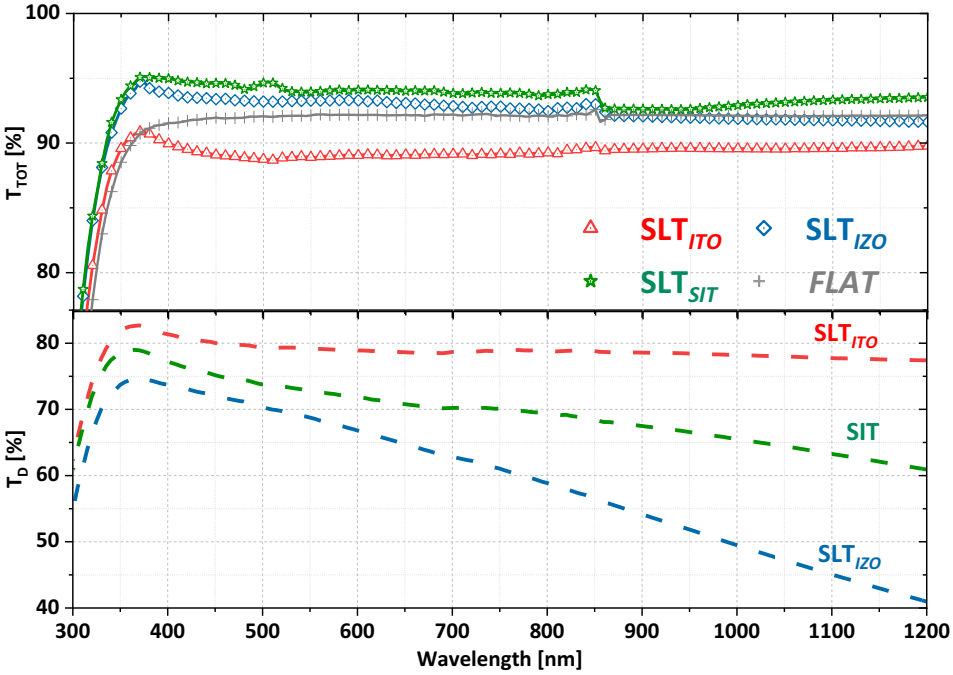

FIGURE 14 | Total transmission spectra (solid line with symbols) and diffused transmission spectra (dashed lines) of SLT_{ITO}, SLT_{IZO} and *SIT*.

3.4 | Total Transmission of SLT_{ITO}, SLT_{IZO} and *SIT*

The total transmission (T_{TOT}) spectra (solid line with symbols) and diffused transmission spectra (dashed line) of different textures when probed from the flat side are shown in Figure 14. SLT_{ITO} (red curve) shows a lower transmission for all wavelengths compared with FLAT. This suggests that when we introduce a texture with $S \gg \lambda$ on a flat glass, the transmission at the glass/ air interface of the sample decreases. The light incoming from the nontextured side of the glass interacts with the curved interface of SLT_{ITO} as 'locally flat' due to its feature diameter. The interaction of microtextured glass at this interface follows coherent reflection and obeys Fresnel's relations of reflection coefficients for light entering an optically rarer medium at angles > 0° [49]. With an increased surface area, this texture reflects more light than a flat surface. Interestingly, a weak interference fringe appears for all SLT_{ITO} samples around 350 nm, which is absent in the transmission measurement of FLAT. The small textures of SLT_{IZO} reduce reflection at the glass/ air interface when compared with FLAT. For SLT_{IZO}, the small features ($S \sim \lambda$) aid in breaking the coherence at the glass/air interface. The light scattering is based on incoherent diffraction and follows the Mie scattering mechanism. The total transmission of SLT_{IZO} is greater than that of both SLT_{ITO} and FLAT. When the small features of SLT_{IZO} are superimposed over SLT_{ITO}, a diffractive nature is added to the optical response. The resultant surface (i.e., *SIT*) no longer acts as 'locally flat' (in comparison with SLT_{ITO}). As observed in Figure 11 Zone 2, *SIT* possess the highest amount of small-scale features among the three textures. For *SIT*, the incoherent diffraction scattering dominates the transmission mechanism and as a result, *SIT* exhibits the highest transmission spectrum among the three textures.

The interaction of light with textures is determined by their σ_{rms}, surface vector angles and crater shapes. These observations suggest that to combine two textures, the large and small craters should have distinct, well-defined roughness ranges for which they perform best individually. These ranges must belong to optically refractive and diffractive regimes. As observed in this work, optically, this approach yields the least reflectance while also facilitating effective light diffusion.

3.5 | Solar Cells on Textures

The performances of nc-Si single-junction solar cell devices fabricated on SLT_{ITO}, *SIT* and SLT_{IZO} in superstrate configuration are compared. A solar cell is also made on FLAT as a reference to the textured glass. The performance of solar cells on different textures is shown in Figure 15a–c. The performance parameters of each superstrate solar cell are summarised in Table 2. The tabulated values represent the average performance of the top ten solar cells (out of 30) for each sample. Selected solar cells, their position on the superstrate and standard deviation (SD) are included in the supplement of this paper. The SD of σ_{rms} and the external parameters suggest that the texture properties and their effect on cell performances are homogeneous over the glass strip (3 cm × 10 cm) used in this experiment. *SIT* solar cells showed the highest power conversion efficiency (η) among the differently textured solar cells. The η of *SIT* solar cells is 0.57%, 1.52% and 2.71% (absolute) more than SLT_{ITO}, SLT_{IZO} and FLAT solar cells, respectively. $J_{sc,EQE}$ of *SIT* solar cells was significantly higher than the other two textured solar cells. *SIT* sample outperforms the next best (SLT_{ITO}) by 0.94 mA/cm2. Interestingly, V_{OC} and FF values of *SIT*, SLT_{ITO} are in the same range, whereas V_{OC} and FF values of SLT_{IZO} and FLAT were considerably lower. The efficiency of FLAT is lower than the reported values for n-i-p substrate cells on flat glass, as seen in [21]. While the V_{OC} and J_{SC} values are comparable, the performance drop is primarily

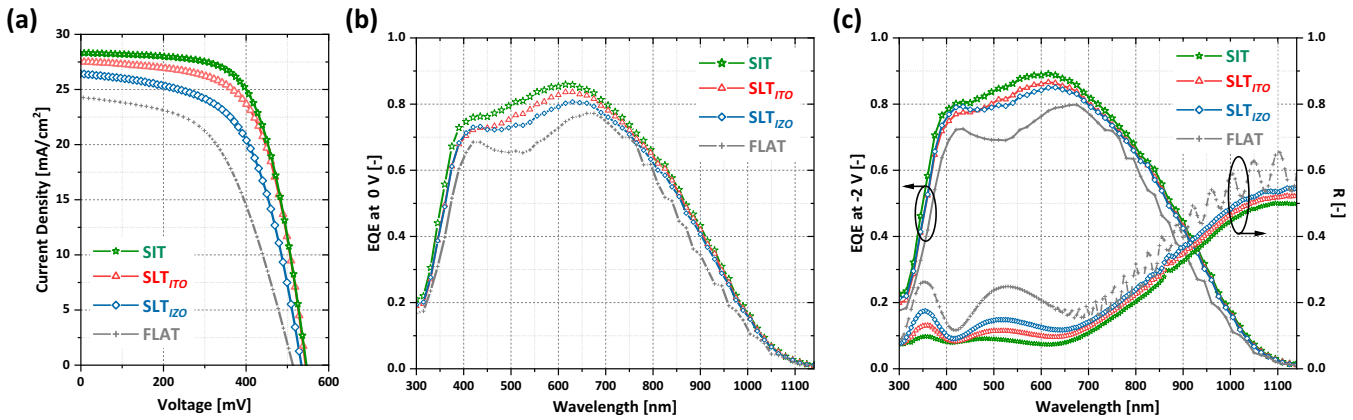

FIGURE 15 | (a) Current density versus voltage characterisation of solar cells on each texture, (b) EQE at 0-V bias, (c) EQE at 2-V reverse bias and reflectance (R) as a function of wavelength for the solar cells.

TABLE 2 | External parameters of solar cells deposited on different textured glass samples. The reported values are calculated from 10 cells on each textured substrate which has highest $V_{oc} \times$ FF value. SD of superstrate σ_{rms} is calculated from four different area AFM scans on same sample.

Sample	σ_{rms} (nm)	V_{oc} (mV)	χ_c (%)	$J_{sc,EQE(0V)}$ (mA/cm2)	$J_{sc,EQE(-2V)}$ (mA/cm2)	$\Delta J_{sc,EQE(-2V,0V)}$ (mA/cm2)	FF (%)	R_s (Ω.cm2)	R_p (kΩ.cm2)	η (%)
SLT_{ITO}	958 ± 22	540	57	25.81	26.84	1.03	63.2	11.0	2.8	8.81
SLT_{IZO}	318 ± 12	534	58	25.08	26.53	1.45	58.7	13.9	1.7	7.86
SIT	416 ± 8	544	57	26.75	27.69	0.94	64.5	9.0	2.7	9.38
FLAT	—	521	63	23.06	24.08	1.02	55.5	13.7	1.0	6.67

due to a low FF. The values of FF reported here on superstrate configuration solar cells in this study, for 3-μm-thick nc-Si:H single-junction solar cells, are close to the observed values by Tan et al. for identical p-i-n configuration and thickness [22]. The electrical losses through series resistances can be further reduced with a thicker IOH as the front electrode.

3.5.1 | Photocurrent Density

The optical properties of textures explained in the previous Sections 3.2–3.4 account for the reflection of the air/glass/air system with two interfaces. In the solar cells, the refractive index of the layers is graded. Four intermediate interfaces of air/glass/IOH/nc-Si:H solar cell/silver architecture are decisive in determining the reflection spectrum of a solar cell. Figure 15c shows the reflectance spectrum of the solar cells. Two major optical Fabry–Perot cavities [50] were observed in the solar cell stack, giving rise to interference fringes in the spectra [51, 52]: (i) the fringe in the visible wavelengths and (ii) fringes in the near-IR wavelength.

i. The fringes with minima at 350 and 525 nm are related to the interference in the TCO layer (by reflection at the IOH/silicon interface). We observe that with changes in the thickness of the IOH, the minima of this fringe shift. This is shown in the Supporting Information of this paper. Cross-sectional SEM images of solar cell (Figure 16) suggest that at the mentioned deposition conditions, the 150-nm layer of sputtered IOH is conformal and does not influence the crater shape. Examining the interfaces as discrete changes in refractive indices ($n_{IOH} - n_{glass}$ and $n_{silicon} - n_{IOH}$), the IOH/silicon interface makes the dominant contribution to the reflection losses. The superstrate σ_{rms} with respect to the thickness of the IOH front electrode determines the R and amplitude of interference fringes in the visible spectrum for these solar cells [51]. For SLT_{ITO}, the $\sigma_{rms} \gg$ IOH thickness. For *SIT*, the $\sigma_{rms} >$ IOH thickness. Whereas for SLT_{IZO}, $\sigma_{rms} \sim$ IOH thickness, which implies the interface is relatively flat for SLT_{IZO}. In solar cells, the overall reflection losses (R) and fringe amplitude follow the same order as σ_{rms}: $FLAT > SLT_{IZO} > SLT_{ITO} > SIT$.

ii. The Fabry–Perot interference beyond 700 nm in the near-IR region is correlated to reflections in the nc-Si:H bulk absorber layer. Compared with FLAT, all three textures on glass have almost nullified the fringes induced by the nc-Si:H. This is because the solar cells on FLAT have flat interfaces for the absorber layer and back reflector, which are unable to break the optical cavity formed. With the introduction of textures to solar cells, the specular component decreases considerably, quenching the interference fringes in EQE and R.

SIT improves the QE in near UV, visible and near-IR ranges in comparison with other textures (Figure 15b). The gain is primarily due to the reduction in R combined with the scattering properties of features. The overall response of the solar cell can be further improved using an external antireflection coating

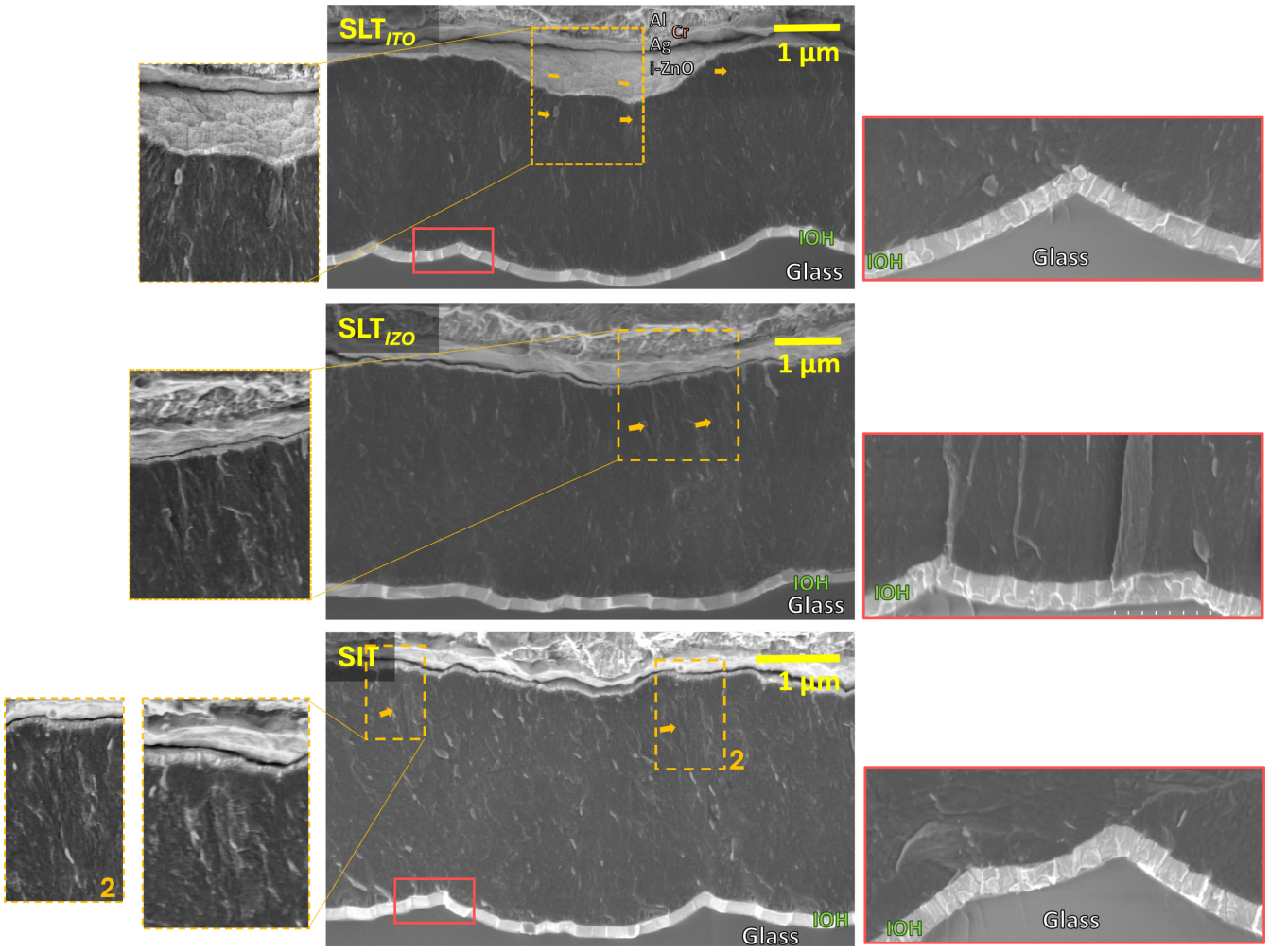

FIGURE 16 | Cross-sectional images of superstrate p-i-n solar cells made on SLT_{ITO}, SLT_{IZO}, SIT. The direction of cell deposition is from the glass (marked) to the top. Defective filaments in the nc-Si bulk are identified and marked with arrows (gold) and zoomed in (gold boxes). IOH conformality is qualitatively examined at different crater shapes and zoomed in (red boxes).

[53, 54]. The spectral utilisation at long wavelengths near IR is affected by the back reflector properties. From the SEM image in Figure 16, it is observed that the back reflector surface morphology is rather flat and not an exact repetition of the textures on glass after a deposition of a very thick nc-Si:H layer. The spectral utilisation in the near IR can be further increased with increasing χ_c [45], but this often causes a drop in V_{oc}. Sai et al. and Guha et al. have reported an EQE of ≈0.3 at $\lambda = 1000$ nm for their record devices at high χ_c values with a $V_{oc} \approx$ of 480 mV [54, 55].

To add results into perspective, Tan et al. had reported the highest J_{sc} for the superstrate configuration single texture at $\sigma_{rms} = 126$ nm, achieving 27.7 mA/cm2, but at the cost of FF and V_{OC}, resulting in $\eta = 7.4\%$ [26]. Also, $\eta = 10.2\%$ is reported in the same paper at a $\sigma_{rms} = 370$ nm and a J_{sc} of 25.6 mA/cm2 [26]. For a TCO (5µm thick)-based pyramidal texture approach on flat glass (σ_{rms} not available), the highest reported η is 10.9% at a J_{sc} of 27.5 mA/cm2 [56] by EPFL. A similar TCO-based MST approach on periodic honeycomb textures on glass has also been reported for two-junction tandem solar cells, with a total spectral utilisation of approximately 26.0 mA/cm2 [57]. For a periodic honeycomb texture on glass with IOH (150 nm), a spectral utilisation of 28.6 mA/cm2 is reported by TU Delft [58] in superstrate p-i-n configuration. It has been a point of long discussion whether the substrate or the superstrate configuration is beneficial from a conversion efficiency perspective [59, 60]. Still, from an optical standpoint, the substrate configuration has an inherent advantage in that it does not have a smooth glass (or similar transparent material) acting as an extra reflective layer at the front of solar cells. In the substrate n-i-p configuration, the main component to be optimised is the back reflector texture. The highest reported η values on the substrate n-i-p nc-Si:H solar cells are 11.9% with $J_{sc} = 28.74$ by AIST, Japan [61, 62] on honeycomb textures developed on wafers with moth eye antireflection coatings [54]. Additionally, a very high J_{sc} of 32.9 mA/cm2 is reported on a honeycomb textured wafer [53].

3.5.2 | nc-Si:H Absorber Quality

Cross-section SEM images of solar cells are shown in Figure 16. For a 3-µm-thick nc-Si:H absorber, we observe a few cracks (or voids) near the back contact of the solar cells. Cracks are formed in the crystalline absorber due to the shadowing effect at narrow funnel-shaped growth regions [53, 63]. This crack formation is dependent on the thickness of the cell and the slope of the

superstrate, at which silicon is deposited [7]. These cracks act as sites for charge carrier recombination and low parallel resistance, leading to low FF. Figure 15b shows the EQE of solar cells at 0 V, and Figure 15c shows EQE of solar cells at a reverse bias voltage of 2 V. The absolute difference between EQE measurements at 0- and −2-V bias is representative of the recombination losses in the at defect rich filaments in solar cell [64]. From the $\Delta J_{sc,EQE(-2V,0V)}$ values tabulated in Table 2, SLT_{IZO} has the most recombination losses in the bulk, this is presumably because of the sharp angles of SLT_{IZO} with its 'V shape' craters. The ΔJ_{sc} is significant in the blue response as well, indicating an electron recombination in the vicinity of the p/i interface of the cell. These recombinations lead to low V_{OC} values. As a consequence of the bulk defects, V_{OC} and FF values also follow the order of angle distribution: $SIT > SLT_{ITO} > SLT_{IZO} > FLAT$. Python et al. have made a similar discussion on how the U-type superstrate mitigates crack formation when compared with Asahi V-type superstrates [65]. We speculate that *SIT* has the added advantage of smoother crater boundaries owing to the double etching step involved in making *SIT*. This suppresses the density of recombination centres in the solar cell [9]. However, to make a conclusion on this effect in *SIT*, more statistics are required.

4 | Conclusion

This work presents a detailed sample study of three sacrificial random texturing approaches on glass utilising two different sacrificial TCO layers, namely, ITO and i-ZnO. i-ZnO is a novel TCO material used in texturing glass. The paper presents observations on the physical properties of the created textures and their interaction with light. Using the ITO layer for sacrificial texturing (SLT_{ITO}) resulted in large craters with spherical 'inverted U' shapes, and the i-ZnO sacrificial layer (SLT_{IZO}) created small craters with conical 'inverted V' shapes. A correlation is observed between the RMS roughness of the textures and their diffused transmission. We combine the processing conditions of optically best-diffusing textures from each sample set to make a superimposed texturing—*SIT*. Large-size textures of SLT_{ITO} follow coherent refraction, while SLT_{IZO} nanotextures follow incoherent Mie scattering. *SIT* has features resembling its constituent morphologies and exhibits combined scattering characteristics of both diffractive and refractive scattering regimes across a broad wavelength. *SIT* exhibits excellent optical properties in terms of reflectance and scattering. The nc-Si:H single-junction solar cells made on *SIT* resulted in the highest performing solar cell in terms of EQE and η among the mentioned textures.

Author Contributions

Govind Padmakumar: conceptualization (lead), data curation (lead), formal analysis (lead), investigation (lead), methodology (lead), visualization (lead), writing – original draft (lead). **Matthias Criel:** data curation (supporting), formal analysis (supporting), project administration (supporting), resources (supporting). **Tanya Kashyap:** data curation (supporting), formal analysis (supporting). **Federica Saitta:** resources (supporting). **Paula Perez-Rodriguez:** investigation (supporting), resources (supporting), writing – review and editing (supporting). **René A. C. M. M. van Swaaij:** writing – review and editing (supporting). **Arno H. M. Smets:** conceptualization (supporting), formal analysis (supporting), funding acquisition (lead), supervision: (lead), writing – review and editing (equal).

Acknowledgements

The authors acknowledge financial and technical support from HyET Solar Netherlands B.V., Arnhem, The Netherlands.

Funding

The authors acknowledge financial and technical support from HyET Solar Netherlands B.V., Arnhem, The Netherlands.

Conflicts of Interest

The authors declare no conflicts of interest.

Data Availability Statement

The data that support the findings of this study are available from the corresponding author upon reasonable request.

References

1. H. W. Deckman, C. R. Wronski, H. Witzke, and E. Yablonovitch, "Optically Enhanced Amorphous Silicon Solar Cells," *Applied Physics Letters* 42, no. 11 (1983): 968–970, https://doi.org/10.1063/1.93817.

2. A. R. Pascoe, S. Meyer, W. Huang, et al., "Enhancing the Optoelectronic Performance of Perovskite Solar Cells via a Textured $CH_3NH_3PbI_3$ Morphology," *Advanced Functional Materials* 26, no. 8 (2016): 1278–1285, https://doi.org/10.1002/adfm.201504190.

3. C. Onwudinanti, R. Vismara, O. Isabella, L. Grenet, F. Emieux, and M. Zeman, "Advanced Light Management Based on Periodic Textures for Cu(In,Ga)Se_2 Thin-Film Solar Cells," *Optics Express* 24, no. 6 (2016): A693, https://doi.org/10.1364/OE.24.00A693.

4. X. Luo, H. Luo, H. Li, et al., "Efficient Perovskite/Silicon Tandem Solar Cells on Industrially Compatible Textured Silicon," *Advanced Materials* 35, no. 9 (2023): 2207883, https://doi.org/10.1002/adma.202207883.

5. O. Isabella, J. Krc, and M. Zeman, "Modulated Surface Textures for Enhanced Light Trapping in Thin-Film Silicon Solar Cells," *Applied Physics Letters* 97, no. 10 (2010): 101106, https://doi.org/10.1063/1.3488023.

6. R. J. D. Tilley, *Colour and the Optical Properties of Materials* (John Wiley & Sons Ltd, 2011).

7. D. Y. Kim, S. Hänni, J. W. Schüttauf, R. A. van Swaaij, and M. Zeman, "Quantification of Valleys of Randomly Textured Substrates as a Function of Opening Angle: Correlation to the Defect Density in Intrinsic nc-Si:H," *ACS Applied Materials and Interfaces* 8, no. 32 (2016): 20660–20666, https://doi.org/10.1021/acsami.6b03995.

8. G. Yang, R. A. van Swaaij, H. Tan, O. Isabella, and M. Zeman, "Modulated Surface Textured Glass as Substrate for High Efficiency Microcrystalline Silicon Solar Cells," *Solar Energy Materials and Solar Cells* 133 (2015): 156–162, https://doi.org/10.1016/j.solmat.2014.11.013.

9. H. B. Li, R. H. Franken, J. K. Rath, and R. E. Schropp, "Structural Defects Caused by a Rough Substrate and Their Influence on the Performance of Hydrogenated Nano-Crystalline Silicon n-i-p Solar Cells," *Solar Energy Materials and Solar Cells* 93, no. 3 (2009): 338–349, https://doi.org/10.1016/j.solmat.2008.11.013.

10. H. Sai, K. Maejima, T. Matsui, et al., "Impact of Front TCO Layer in Substrate-Type Thin-Film Microcrystalline Silicon Solar Cells," in *2015 IEEE 42nd Photovoltaic Specialist Conference (PVSC)*, 2015 (2015): (IEEE), 1–6, https://doi.org/10.1109/PVSC.2015.7355677.

11. H. Sai, K. Maejima, T. Matsui, et al., "High-Efficiency Microcrystalline Silicon Solar Cells on Honeycomb Textured Substrates Grown

With High-Rate VHF Plasma-Enhanced Chemical Vapor Deposition," *Japanese Journal of Applied Physics* 54, no. 8S1 (2015): 08KB05, https://doi.org/10.7567/JJAP.54.08KB05.

12. G. Li, Y. Zhou, and F. Liu, "Influence of Textured c-Si Surface Morphology on the Interfacial Properties of Heterojunction Silicon Solar Cells," *Journal of Non-Crystalline Solids* 358, no. 17 (2012): 2223–2226, https://doi.org/10.1016/j.jnoncrysol.2011.12.106.

13. T. de Vrijer and A. H. M. Smets, "Advanced Textured Monocrystalline Silicon Substrates With High Optical Scattering Yields and Low Electrical Recombination Losses for Supporting Crack-Free Nano- to Poly-Crystalline Film Growth," *Energy Science & Engineering* 9, no. 8 (2021): 1080–1089, https://doi.org/10.1002/ese3.873.

14. M. Python, E. Vallat-Sauvain, J. Bailat, et al., "Relation Between Substrate Surface Morphology and Microcrystalline Silicon Solar Cell Performance," *Journal of non-Crystalline Solids* 354, no. 19–25 (2008): 2258–2262, https://doi.org/10.1016/j.jnoncrysol.2007.09.084.

15. A. Gordijn, M. N. van den Donker, F. Finger, et al., "Flexible a-Si/c-Si Tandem Modules in the Helianthos Project," Tech. rep.

16. G. Bugnon, G. Parascandolo, T. Söderström, et al., "A New View of Microcrystalline Silicon: The Role of Plasma Processing in Achieving a Dense and Stable Absorber Material for Photovoltaic Applications," *Advanced Functional Materials* 22, no. 17 (2012): 3665–3671, https://doi.org/10.1002/adfm.201200299.

17. P. K. Gupta, "Non-Crystalline Solids: Glasses and Amorphous Solids," Tech. rep. (1996).

18. G. Padmakumar, A. Balaji, M. Criel, et al., "Engineering of Hexagonal Microtextures on Glass," *ACS Applied Optical Materials* 3, no. 10 (2025): 2360–2372, https://doi.org/10.1021/acsaom.5c00328.

19. H. Park, S. M. Iftiquar, M. Shin, et al., "Fabrication of Honeycomb Textured Glass Substrate and Nanotexturing of Zinc Oxide Front Electrode for Its Application in High Efficiency Thin Film Amorphous Silicon Solar Cell," *Journal of Photonics for Energy* 7, no. 2 (2017): 025502, https://doi.org/10.1117/1.jpe.7.025502.

20. P. I. Widenborg and A. G. Aberle, "Polycrystalline Silicon Thin-Film Solar Cells on AIT-Textured Glass Superstrates," *Advances in OptoElectronics* 2007 (2007): 24584, https://doi.org/10.1155/2007/24584.

21. G. Yang, R. A. C. M. M. van Swaaij, O. Isabella, and M. Zeman, "A Novel Way of Texturing Glass for Microcrystalline Silicon Thin Film Solar Cells Application," *Progress in Photovoltaics: Research and Applications* 23, no. 10 (2015): 1283–1290, https://doi.org/10.1002/pip.2550.

22. H. Tan, E. Psomadaki, O. Isabella, et al., "Micro-Textures for Efficient Light Trapping and Improved Electrical Performance in Thin-Film Nanocrystalline Silicon Solar Cells," *Applied Physics Letters* 103, no. 17 (2013): 173905, https://doi.org/10.1063/1.4826639.

23. B. J. Wiley, D. Qin, and Y. Xia, "Nanofabrication at High Throughput and Low Cost," *ACS Nano* 4, no. 7 (2010): 3554–3559, https://doi.org/10.1021/nn101472p.

24. O. Kluth, G. Schöpe, J. Hüpkes, C. Agashe, J. Müller, and B. Rech, "Modified Thornton Model for Magnetron Sputtered Zinc Oxide: Film Structure and Etching Behaviour," *Thin Solid Films* 442, no. 1–2 (2003): 80–85, https://doi.org/10.1016/S0040-6090(03)00949-0.

25. M. L. Addonizio, L. Fusco, A. Antonaia, F. Cominale, and I. Usatii, "Optimization of Surface Morphology and Scattering Properties of TCO/AIT Textured Glass Front Electrode for Thin Film Solar Cells," *Applied Surface Science* 357 (2015): 651–658, https://doi.org/10.1016/j.apsusc.2015.09.073.

26. H. Tan, E. Moulin, F. T. Si, et al., "Highly Transparent Modulated Surface Textured Front Electrodes for High-Efficiency Multijunction Thin-Film Silicon Solar Cells," *Progress in Photovoltaics: Research and Applications* 23, no. 8 (2015): 949–963, https://doi.org/10.1002/pip.2639.

27. H. Sai, K. Saito, N. Hozuki, and M. Kondo, "Relationship Between the Cell Thickness and the Optimum Period of Textured Back Reflectors in Thin-Film Microcrystalline Silicon Solar Cells," *Applied Physics Letters* 102, no. 5 (2013): 053509, https://doi.org/10.1063/1.4790642.

28. H. Sai, T. Koida, T. Matsui, I. Yoshida, K. Saito, and M. Kondo, "Microcrystalline Silicon Solar Cells With 10.5% Efficiency Realized by Improved Photon Absorption via Periodic Textures and Highly Transparent Conductive Oxide," *Applied Physics Express* 6, no. 10 (2013): 104101, https://doi.org/10.7567/APEX.6.104101.

29. Corning Incorporated, "Semiconductor Glass Wafers Product Information Sheet," Tech. rep. (2015).

30. Corning Incorporated, "Exceptional Dimensional Stability and Surface Quality in Thin, Large-Size Sheets," Tech. rep. (2021).

31. O. Tuna, Y. Selamet, G. Aygun, and L. Ozyuzer, "High Quality ITO Thin Films Grown by dc and RF Sputtering Without Oxygen," *Journal of Physics D: Applied Physics* 43, no. 5 (2010): 055402, https://doi.org/10.1088/0022-3727/43/5/055402.

32. K. H. Patel and S. K. Rawal, "Influence of Power and Temperature on Properties of Sputtered AZO Films," *Thin Solid Films* 620 (2016): 182–187, https://doi.org/10.1016/j.tsf.2016.08.073.

33. M. Nisha, S. Anusha, A. Antony, R. Manoj, and M. K. Jayaraj, "Effect of Substrate Temperature on the Growth of ITO Thin Films," *Applied Surface Science* 252, no. 5 (2005): 1430–1435, https://doi.org/10.1016/j.apsusc.2005.02.115.

34. G. Frank and H. Köstlin, "Applied so Electrical Properties and Defect Model of Tin-Doped Indium Oxide Layers," Tech. rep. (1982).

35. A. H. M. Smets, *Growth Related Material Properties of Hydrogenated Amorphous Silicon* (Technische Universiteit Eindhoven, 2002), https://doi.org/10.6100/IR556557.

36. J. M. Bennett and L. Mattsson, *Introduction to Surface Roughness and Scattering* (Optical Society of America, 1989), https://doi.org/10.1364/1557521085.

37. K. Jäger, O. Isabella, L. Zhao, and M. Zeman, "Light Scattering Properties of Surface-Textured Substrates," *Physica Status Solidi (C)* 7, no. 3–4 (2010): 945–948, https://doi.org/10.1002/pssc.200982695.

38. K. Jäger, O. Isabella, R. A. C. M. M. van Swaaij, and M. Zeman, "Angular Resolved Scattering Measurements of Nano-Textured Substrates in a Broad Wavelength Range," *Measurement Science and Technology* 22, no. 10 (2011): 105601, https://doi.org/10.1088/0957-0233/22/10/105601.

39. H. Scherg-Kurmes, S. Seeger, S. Körner, B. Rech, R. Schlatmann, and B. Szyszka, "Optimization of the Post-Deposition Annealing Process of High-Mobility In_2O_3:H for Photovoltaic Applications," *Thin Solid Films* 599 (2016): 78–83, https://doi.org/10.1016/j.tsf.2015.12.054.

40. C. Battaglia, L. Erni, M. Boccard, et al., "Micromorph Thin-Film Silicon Solar Cells With Transparent High-Mobility Hydrogenated Indium Oxide Front Electrodes," *Journal of Applied Physics* 109, no. 11 (2011): 114501, https://doi.org/10.1063/1.3592885.

41. S. Faý, L. Feitknecht, R. Schlüchter, U. Kroll, E. Vallat-Sauvain, and A. Shah, "Rough ZnO Layers by LP-CVD Process and Their Effect in Improving Performances of Amorphous and Microcrystalline Silicon Solar Cells," *Solar Energy Materials and Solar Cells* 90, no. 18–19 (2006): 2960–2967, https://doi.org/10.1016/j.solmat.2006.06.003.

42. M. L. Addonizio and C. Diletto, "Doping Influence on Intrinsic Stress and Carrier Mobility of LP-MOCVD-Deposited ZnO:B Thin Films," *Solar Energy Materials and Solar Cells* 92, no. 11 (2008): 1488–1494, https://doi.org/10.1016/j.solmat.2008.06.013.

43. M. N. van den Donker, B. Rech, F. Finger, L. Houben, W. M. M. Kessels, and M. C. M. van de Sanden, "Deposition of Highly Efficient Microcrystalline Silicon Solar Cells Under Conditions of Low H_2 Dilution: The Role of the Transient Depletion Induced Incubation Layer,"

Progress in Photovoltaics: Research and Applications 15, no. 4 (2007): 291–301, https://doi.org/10.1002/pip.743.

44. O. Vetterl, F. Finger, R. Carius, et al., "Intrinsic Microcrystalline Silicon: A New Material for Photovoltaics," *Solar Energy Materials & Solar Cells* 62, no. 1/2 (2000): 97.

45. M. van den Donker, B. Rech, R. Schmitz, et al., "Hidden Parameters in the Plasma Deposition of Microcrystalline Silicon Solar Cells," *Journal of Materials Research* 22, no. 7 (2007): 1767–1774, https://doi.org/10.1557/jmr.2007.0226.

46. A. Krywonos, J. E. Harvey, and N. Choi, "Linear Systems Formulation of Scattering Theory for Rough Surfaces With Arbitrary Incident and Scattering Angles," Tech. rep. (2011).

47. K. Jäger, R. A. C. M. M. van Swaaij, and M. Zeman, "The Scalar Scattering Theory: A Multi-Functional Tool for Optimizing Scattering in Thin-Film Silicon Solar Cells," in *Renewable Energy and the Environment Optics and Photonics Congress* (OSA, 2012): PT3C.7, https://doi.org/10.1364/PV.2012.PT3C.7.

48. A. H. Smets, W. M. Kessels, and M. C. van de Sanden, "Temperature Dependence of the Surface Roughness Evolution During Hydrogenated Amorphous Silicon Film Growth," *Applied Physics Letters* 82, no. 6 (2003): 865–867, https://doi.org/10.1063/1.1543237.

49. A. H. Smets, K. Jäger, I. Olindo, M. Zeman, and R. A. van Swaaij, *Solar Energy: The Physics and Engineering of Photovoltaic Conversion, Technologies and Systems* (UIT Cambridge, 2016).

50. H. Eugene, *Optics*, 4th ed. (Addison-Wesley, 2002).

51. A. Larena, F. Millán, G. Pérez, and G. Pinto, "Effect of Surface Roughness on the Optical Properties of Multilayer Polymer Films," Tech. rep. (2002).

52. A. Larena, G. Pinto, and F. Millán, "Using the Lambert-Beer Law for Thickness Evaluation of Photoconductor Coatings for Recording Holograms," Tech. rep. (1995).

53. T. Matsui, H. Sai, A. Bidiville, H.-J. Hsu, and K. Matsubara, "Progress and Limitations of Thin-Film Silicon Solar Cells," *Solar Energy* 170 (2018): 486–498, https://doi.org/10.1016/j.solener.2018.05.077.

54. H. Sai, T. Matsui, K. Saito, M. Kondo, and I. Yoshida, "Photocurrent Enhancement in Thin-Film Silicon Solar Cells by Combination of Anti-Reflective Sub-Wavelength Structures and Light-Trapping Textures," *Progress in Photovoltaics: Research and Applications* 23, no. 11 (2015): 1572–1580, https://doi.org/10.1002/pip.2594.

55. S. Guha, J. Yang, and B. Yan, "High Efficiency Multi-Junction Thin Film Silicon Cells Incorporating Nanocrystalline Silicon," *Solar Energy Materials and Solar Cells* 119 (2013): 1–11, https://doi.org/10.1016/j.solmat.2013.03.036.

56. S. Hänni, G. Bugnon, G. Parascandolo, et al., "High-Efficiency Microcrystalline Silicon Single-Junction Solar Cells," *Progress in Photovoltaics: Research and Applications* 21, no. 5 (2013): 821–826, https://doi.org/10.1002/pip.2398.

57. H. Park and D. Kim, "Influence on the Haze Effect of Si Thin-Film Solar Cell on Multi-Surface Textures of Periodic Honeycomb Glass," *Transactions on Electrical and Electronic Materials* 22, no. 1 (2021): 80–90, https://doi.org/10.1007/s42341-020-00263-3.

58. G. Padmakumar, F. Saitta, P. Sluijs, et al., "Progress in the Research on the Performance, Processing and Reliability of Lightweight and Flexible Thin-Film PV Foils at TUDelft," in *2025 IEEE 53rd Photovoltaic Specialists Conference (PVSC)* (IEEE, 2025), 1124–1126, https://doi.org/10.1109/PVSC59419.2025.11133203.

59. K. H. Kim, S. Kasouit, E. V. Johnson, and P. R. I. Cabarrocas, "Substrate Versus Superstrate Configuration for Stable Thin Film Silicon Solar Cells," *Solar Energy Materials and Solar Cells* 119 (2013): 124–128, https://doi.org/10.1016/j.solmat.2013.05.045.

60. F. J. Haug and C. Ballif, "Light Management in Thin Film Silicon Solar Cells," *Energy & Environmental Science* 8 (2015): 824–837, https://doi.org/10.1039/c4ee03346a.

61. H. Sai, T. Matsui, and K. Matsubara, "Key Points in the Latest Developments of High-Efficiency Thin-Film Silicon Solar Cells," *Physica Status Solidi (A)—Applications and Materials Science* 214, no. 12 (2017): 1700544, https://doi.org/10.1002/pssa.201700544.

62. H. Sai, T. Matsui, H. Kumagai, and K. Matsubara, "Thin-Film Microcrystalline Silicon Solar Cells: 11.9% Efficiency and Beyond," *Applied Physics Express* 11, no. 2 (2018): 022301, https://doi.org/10.7567/APEX.11.022301.

63. M. Python, D. Dominé, T. Söderström, F. Meillaud, and C. Ballif, "Microcrystalline Silicon Solar Cells: Effect of Substrate Temperature on Cracks and Their Role in Post-Oxidation," *Progress in Photovoltaics: Research and Applications* 18, no. 7 (2010): 491–499, https://doi.org/10.1002/pip.956.

64. G. Yue, L. Sivec, J. M. Owens, B. Yan, J. Yang, and S. Guha, "Optimization of Back Reflector for High Efficiency Hydrogenated Nanocrystalline Silicon Solar Cells," *Applied Physics Letters* 95, no. 26 (2009): 263501, https://doi.org/10.1063/1.3279143.

65. M. Python, C. Ballif, F. Meillaud, O. Madani, and D. Domine, "Influence of the Substrate Geometrical Parameters on Microcrystalline Silicon Growth for Thin-Film Solar Cells," *Solar Energy Materials and Solar Cells* 93 (2009): 1714–1720, https://doi.org/10.1016/j.solmat.2009.05.025.

Supporting Information

Additional supporting information can be found online in the Supporting Information section. Superimposed_Sacrificial_Texturing_to_Enhance_the_Optical_Performance_of_Thin_Film_Solar_Cells_R2_GvP_Supplementary data.pdf.